Nanometre-thick Si/Al Gradient Materials for Sustainable Spin Current Generation

Taisuke Horaguchi
  Keio University

Cong He
  National Institute for Materials Science

Zhenchao Wen
  National Institute for Materials Science (NIMS)   https://orcid.org/0000-0001-7496-1339

Tadakatsu Ohkubo
  National Institute for Materials Science

Kazuhiro Hono
  National Institute for Materials Science   https://orcid.org/0000-0001-7367-0193

Seiji Mitani
  NIMS

Hiroaki Sukegawa
  National Institute for Materials Science

Junji Fujimoto
  Kavli Institute for Theoretical Sciences

Kazuto Yamanoi
  Keio University

Mamoru Matsuo
  Kavli Institute for Theoretical Sciences   https://orcid.org/0000-0003-1303-7614

Yukio Nozaki (✉ nozaki@phys.keio.ac.jp)
  Keio University

Article

Nanometre-thick Si/Al Gradient Materials for Sustainable Spin Current Generation

Taisuke Horaguchi[1], Cong He[2], Zhenchao Wen[2], Tadakatsu Ohkubo[2], Kazuhiro Hono[2], Seiji Mitani[2], Hiroaki Sukegawa[2], Junji Fujimoto[3], Kazuto Yamanoi[1], Mamoru Matsuo[3,4,5,6], and Yukio Nozaki[1,7,*]

[1]Department of Physics, Keio University, Yokohama 223-8522, Japan
[2]Research Center for Magnetic and Spintronic Materials, National Institute for Materials Science, 1-2-1 Sengen, Tsukuba, Ibaraki 305-0047, Japan.
[3]Kavli Institute for Theoretical Sciences, University of Chinese Academy of Sciences, No.3, Nanyitiao, Zhongguancun, Haidian District, Beijing, China.
[4]CAS Center for Excellence in Topological Quantum Computation, University of Chinese Academy of Sciences, Beijing 100190, China.
[5]RIKEN Center for Emergent Matter Science (CEMS), Wako, Saitama 351-0198, Japan.
[6]Advanced Science Research Center, Japan Atomic Energy Agency, Tokai, 319-1195, Japan.
[7]Center for Spintronics Research Network, Keio University, Yokohama 223-8522, Japan
[*]e-mail: nozaki@phys.keio.ac.jp

ABSTRACT

Green materials for electron spin manipulation are essential for common spintronic applications. Recent studies have documented the efficient generation of spin torque using spin-orbit interactions (SOIs); however, SOI use relies on the employment of rare metals such as platinum. Here, we demonstrate that a nanometre-thick gradient from silicon to aluminium, which consists of readily available elements from earth resources, can produce a spin torque over three times as large as that of platinum, despite the weak SOI of these compositions. The spin-torque efficiency can be improved by decreasing the thickness of the gradient, while a sharp interface was not found to increase the spin torque. Moreover, the electric conductivity of the gradient material can be up to twice as large as that of platinum, which provides a way to reduce Joule heating losses and signal delays in spintronic device circuits. Our findings represent a pathway for sustainable spin manipulation.

Non-equilibrium spin polarisation in conduction electrons enables the magnetisation direction to be manipulated via spin torque using spin-orbit interactions (SOIs) in spintronic devices such as magnetic random-access memory (MRAM)[1,2] and spin torque nanooscillators[3–5]. Phenomena such as the spin-Hall effect (SHE)[6–10] and the Rashba-Edelstein effect (REE)[11–14] are commonly used to generate spin-polarised flow, i.e. spin currents (SC), in strong SOI materials. Such non-equilibrium spin polarisation generally requires specific materials with a strong SOI, usually consisting of heavy 5d metal elements such as tantalum (Ta), tungsten (W) and platinum (Pt). The figure of merit for SC generation capability is generally determined as the product of the spin Hall angle and the electric conductivity of the material. Namely, higher conductivity materials exhibit superior SC generation, while stronger SOI elements generally exhibit smaller conductivities. This has been observed in hitherto promising candidate materials for generating spin torque in MRAMs, such as $\beta-$Ta and $\beta-$W[15–19]. The material choice dilemma for SC generation creates a bottleneck in spintronic device production. Poor conductivity in SC circuits can lead to other serious problems such as wiring delays and Joule losses in integrated circuits. Moreover, semiconductor device performance is often degraded by contamination with strong SOI elements. Therefore, a SOI-free technology is important for enabling SC circuit integration in electric devices. The problem of rare-metal element scarcity also poses a serious challenge to sustainable development.

A promising technology for producing flow of spin angular momentum without using SOI is spin separation produced by a magnetic field gradient. Stern and Gerlach achieved such separation in 1922 with a spin current generated along a field gradient (z-axis in Fig. 1a)[20,21]. This mechanism can be used to generate a spin current without using SOI. Indeed, it has been experimentally demonstrated that an emergent magnetic field can be produced based on the gyromagnetic effect on spins in metallic liquid[22], thin copper films[23–25], and quark-gluon plasma[26,27]. A similar mechanism was recently proposed in a surface-oxidised copper film[28], where an emergent field was generated by a non-uniform electric current, although its physical

origin is still controversial[29–32]. Because a conductivity gradient leads to a vortical electric current that acts on spins as an emergent magnetic field (Fig. 1b), the magnitude of the field should depend on the thickness of electron conductivity gradient in oxides. However, the thickness of the oxidation gradient is difficult to control atomically. This poses a problem not only for practical applications of spintronic devices but also for confirming the existence of emergent magnetic fields due to electric current vorticity.

In this study, we successfully fabricated a nanometre-thick artificial gradient from silicon (Si) to aluminium (Al), which constitutes the second- and third-most abundant components in the Earth's crust (Fig. 1c), and we demonstrate its ability to generate a spin torque of greater magnitude than Pt. The magnitude of the spin torque increases when the compositional gradient steepens; however, an atomically sharp interface does not significantly increase the spin torque. Moreover, as reported in the study of a surface-oxidised copper (Cu) film[28], we observed a large non-reciprocity that is regarded as evidence for a SC generated via an emergent magnetic field due to electric current vorticity.

Fabrication and structural analysis of Si/Al gradient materials

We fabricated Si(10)/Al($t_i/2$)/ Si($t_i/2$)/Al(10)/Ni$_{95}$Cu$_5$(10)/SiO$_2$(20) (unit: nm) multilayer strips on a thermally oxidised Si substrate by means of a conventional lift-off method using magnetron sputtering and photolithography. Here, t_i is the thickness of the interfacial Al/Si insertion, which varied from 0.5 to 2.0 nm at intervals of 0.5 nm. Al is a very conductive metal with an open 2p shell. Although Si is adjacent to Al in the periodic table, it is a semiconductor with much lower electrical conductivity than Al. Sputter deposition processes generally lead to atomic or metallographic disturbances at an interface due to the large kinetic energy of the sputtered particles. An insertion of a few nm of Al/Si therefore increases the mixed region at the interface between 10-nm-thick Si and Al layers. Indeed, microstructural analysis using high-angle annular dark-field scanning transmission electron microscopy (HAADF-STEM) revealed an increase in the thickness of the compositional gradient from Si to Al with increasing t_i. Figure 2a,b displays cross-sectional HAADF-STEM images near the Si/Al interface with $t_i = 2.0$ and 1.0 nm, respectively. In comparison, a cross-section of a Si/Al interface without Al/Si insertion (i.e. $t_i = 0$ nm) is also shown in Fig. 2c, in which a sharp interface was clearly observed. The Al/Si insertion (with thickness t_i) obscures the Si/Al boundary. Moreover, aggregation of Al and/or Si was observed at the Si/Al interface for $t_i = 2.0$ nm. The formation of such aggregation features is attributed to non-solid solution atomic mixing between Si and Al. Energy dispersive spectroscopy (EDS) line profiles of each element (Si and Al) were obtained by averaging the signals in the dashed box area shown in Fig. 2d,e,f which explicitly confirm the formation of a Si/Al gradient with a transition thickness that systematically varies with t_i. The transparent bold lines in Fig. 2g,h,i show the best fit to the following equation:

$$Composition = \frac{C_1 + C_2}{2} \pm \frac{C_2 - C_1}{2} \tanh\left(\frac{z - z_{int}}{L}\right), \tag{1}$$

where C_1 and C_2 are the composition at each end of an EDS scan, z_{int} is the centre position of the interface, and L is the thickness of the compositional gradient from Si to Al. The fit of Eq. (1) indicates L values of 1.3 and 2.4 nm for $t_i = 1.0$ and 2.0 nm, respectively. As shown in Fig. 2, some compositional fluctuations occur along the interfaces, especially for the sample with $t_i = 2.0$ nm; thus, the value of L depends on both the size and position of the EDS signal-averaging window. The value of L determined in Fig. 2 should be regarded as an averaged thickness of the compositional gradient. It is known that Al and Si form a typical non-solid solution combination at equilibrium. Few intermetallic compound or intermediate phases of these elements exist, although certain non-equilibrium states can form during the sputter deposition process at room temperature. Figures 2j and 2k are nanobeam electron diffraction (NBED) patterns for 10-nm-thick Si and Al layers, respectively. A broad halo pattern from the amorphous structure of the Si layer is present, whereas diffraction spots corresponding to the polycrystalline nature of the Al layer appear in the high-resolution HAADF-STEM image in Fig. 2l.

Electric current-induced spin torque

When an electric current is applied to the bilayer strip consisting of a nonmagnet (NM) and a ferromagnet (FM), part of the SC generated in the NM is transmitted towards the FM followed by a spin torque applied on the magnetisation of the FM. This torque is generally referred to as a damping-like (DL) torque, $\boldsymbol{\tau}_{DL}$, whereas a separate spin torque known as the field-like (FL) torque, $\boldsymbol{\tau}_{FL}$, arises from the SC reflected at the NM/FM interface. The effect of these torques on a magnetisation $\boldsymbol{m}$ produced by a SC with a polarisation $\boldsymbol{\sigma}_s$ is described by the following equation:

$$\boldsymbol{\tau} = \boldsymbol{\tau}_{DL} + \boldsymbol{\tau}_{FL} = \xi_{DL} j_c \frac{\hbar}{2e} \frac{1}{\mu_0 M_s d_{FM}} \boldsymbol{m} \times (\boldsymbol{m} \times \boldsymbol{\sigma}_s) + \xi_{FL} j_c \frac{\hbar}{2e} \frac{1}{\mu_0 M_s d_{FM}} \boldsymbol{m} \times \boldsymbol{\sigma}_s, \tag{2}$$

where ξ_{DL} and ξ_{FL} are the efficiencies of the DL and FL torques with respect to an electric current density j_c, while e, μ_0, and $\hbar$ are the elementary charge, permeability of a vacuum, and the reduced Planck's constant, respectively. M_s and d_{FM}

are the saturation magnetisation and FM thickness, respectively. Both these orthogonal torques play an important role in magnetisation switching, which has been widely investigated in applications for non-volatile magnetoresistive memory and magnetic logic devices.

To evaluate the strength of the spin torque produced by applying an electric current to the sample, we conducted spin-torque ferromagnetic resonance (ST-FMR) measurements[15, 16, 18, 33–35]. The theory of this technique is described in Supplementary note S1. In the ST-FMR experiment, an alternating current was applied to the strip using a microwave with amplitude of 20 dBm and a frequency of 20 GHz. The direct current voltage V_{dc} magnitude due to the ST-FMR excitation was measured while sweeping the external field from 0 to 2.0 T. Figure 3a shows a typical ST-FMR spectrum for $t_i = 0.5$ nm, which can be reproduced by a combination of symmetric- and antisymmetric-Lorentzian functions, as shown in Fig. 3b. From the amplitude ratio between the symmetric- and antisymmetric-Lorenzian components, V_s/V_a, we can evaluate the spin torque efficiency ξ_{FMR}, which is commonly used as a rough estimate of ξ_{DL} when ξ_{FL} is negligible in ST-FMR. From Eq. (S1) in Supplementary note S1 and the value of V_s/V_a for the ST-FMR spectrum at a given resonant field B_r, we obtain $\xi_{FMR} = 0.029 \pm 0.004$ for a sample with $t_i = 0.5$ nm, whose magnitude is about half the value for a Pt(10 nm)/Ni$_{95}$Cu$_5$(10 nm) bilayer film ($\xi_{FMR} = 0.066 \pm 0.005$). Figure 3c shows ξ_{FMR} as a function of t_i. As shown in Fig. 3c, a lower t_i leads to a larger ξ_{FMR}, although the ξ_{FMR} for $t_i = 0$ nm is similar to the value for a reference sample with an Al(10 nm)/Ni$_{95}$Cu$_5$(10 nm) structure fabricated on a thermally oxidised Si substrate. This result implies that most of the SC is produced in the 10-nm-thick Al region via SHE and that a sharp Si/Al interface does not result in additional SC generation. That is, the nanometre-thick gradient from Si to Al is the most important factor for SC generation in the sample.

In general, a large difference in electric conductance between NM and FM means that the contribution of ξ_{FL} cannot be ignored. As shown in Supplementary note S3, both ξ_{DL} and ξ_{FL} can be determined from the dependence of ξ_{FMR} on d_{FM}. Furthermore, the ratio between ξ_{DL} and ξ_{FL} generally depends on the condition of a NM/FM interface, i.e. an Al/Ni$_{95}$Cu$_5$ interface. In other words, the value of ξ_{FL}/ξ_{DL} is independently determined with respect to the thickness of the compositional gradient at the Si/Al interface. Figure 3d contains a plot of ξ_{FMR} as a function of ξ_{DL} and ξ_{FL} that is expected from Eq.(S2) of Supplementary note S3. From the ξ_{DL} and ξ_{FL} values for $t_i = 1.0$ nm in Supplementary note S3, ξ_{FL}/ξ_{DL} was determined to be 3 for the Al/Ni$_{95}$Cu$_5$ interface. The dashed line in Fig. 3d indicates the condition $\xi_{FL}/\xi_{DL} = 3$. The solid circles on the dashed line in Fig. 3d indicate the experimental ξ_{FMR} values obtained in Fig. 3c. The x- and y-axes values for each circle in Fig. 3d therefore represent ξ_{DL} and ξ_{FL} of each t_i, respectively. As shown in Fig. 3d, the magnitudes of both ξ_{DL} and ξ_{FL} clearly increase with decreasing t_i, which is the thickness of the compositional gradient from Si to Al. Surprisingly, the ξ_{DL} value for $t_i = 1.0$ nm reaches a magnitude three times larger than that of Pt; further increase in ξ_{DL} would be expected for $t_i = 0.5$ nm, even though only weak SOI elements, i.e. Si and Al, were used for the NM. The ratio between ξ_{DL} and ξ_{FL} suggests that the reflected SC is three times larger than the transmitted SC. This is attributed to the fact that electric conductivity in the SC absorber, the Ni$_{95}$Cu$_5$ layer, is an order of magnitude smaller than that of the SC injector, or the Al layer. Further increases in ξ_{DL} can therefore be realised using ferromagnetic materials with a higher electrical conductivity than Ni$_{95}$Cu$_5$.

Origin of spin torque accompanied by Si/Al gradient materials

Below we discuss the origin of spin torque in the Si/Al/Ni$_{95}$Cu$_5$ trilayer film. Similarly to a torque generated via SHE and/or REE with an electric current along the x-axis, the variations of V_s and V_a with respect to the direction of the external magnetic field can be explained by assuming that the electron spin is polarised along the y-axis (see Supplementary note S4)[36–38]. In the Si/Al/Ni$_{95}$Cu$_5$ trilayer film, most of the electric current flows not within the Si or Ni$_{95}$Cu$_5$ layer, but in the Al layer because the electric conductivity of Al is much larger. However, the spin torque produced by the electric current flow in the Al layer via SHE can be ignored because the spin Hall angle for bulk Al is only 0.02[8, 39], which is 10 times smaller than the value of ξ_{DL} in our sample with $t_i = 1.0$ nm. Inversion symmetry breaking at the Al/Ni$_{95}$Cu$_5$ interface can also produce a spin torque. However, this effect should be independent of t_i because the atomic and/or structural asymmetry condition at the Al/Ni$_{95}$Cu$_5$ interface is determined by the sequential sputtering processes of Al and Ni$_{95}$Cu$_5$, which are commonly used in all samples. Consequently, the dependence of ξ_{DL} on t_i is not attributed to a spin torque caused by either bulk or interface SOI. An inversion symmetry breaking leading to an orbital angular momentum (OAM) flow is also enhanced at the Si/Al interface by decreasing the transition width and must be strongest at $t_i = 0$ nm, while the smallest ξ_{DL} was observed at $t_i = 0$ nm, as shown in Fig. 3d. Therefore, generation of OAM flow is not the primary cause of the increase in ξ_{DL} for the compositional gradient from Si to Al. Similarly, interface-generated SCs caused by either spin-orbit filtering or spin-orbit precession[40] can also be excluded.

An additional possible explanation for the increase in ξ_{DL} is SC generation from electric current vorticity via spin vorticity coupling (SVC)[22, 23, 41, 42]. A non-uniform distribution of electric current arises in the nanometre-thick Si/Al gradient from the large difference in electrical conductivity between Si and Al. Similarly to the inversion symmetry breaking, the degree of electric current non-uniformity increases with decreasing compositional gradient thickness. Conversely, specular electron scattering, which occurs at sharp interfaces, would create a uniform electric current distribution near the interface. Consequently, the electric current vorticity will be maximised when compositional gradient thickness is comparable to the effective

mean free path of the electron. The optimisation of ξ_{DL} at a certain compositional gradient thickness seems to support the SVC mechanism. Indeed, as shown in Supplementary note S5, the ratio of ξ_{DL} increases with respect to the compositional gradient thickness by a similar order of magnitude to the value obtained by evaluating a simple model based on SVC theory. Fluctuations in the compositional gradient that disrupt the electric current vorticity are likely to be small because the strength of ξ_{DL} clearly scales with the averaged compositional gradient thickness, as shown in Fig. 3d.

Highly non-reciprocal SC generation in Si/Al gradient materials

A highly non-reciprocal conversion between electric current and SC can be considered additional evidence that SVC contributes to SC generation. In the case of typical SOI-based phenomena, both intrinsic and extrinsic spin-dependent scattering sources exist in the material regardless of the applied electric current. On the contrary, the vorticity gradient needed for SC generation via SVC appears only when a net drift velocity exists. Namely, the SC is not accompanied by a net drift velocity and, consequently, cannot be converted into electric current.

To evaluate the conversion efficiency from a SC to electric current, as shown in Supplementary note S6, we measured the inverse SHE due to the SC[43,44], which was produced by applying an alternating magnetic field[45–48]. Figure 4a shows the conversion efficiency $\theta_{j_s \to j_c}$ of the SC to an electric current as a function of ξ_{DL}, which is proportional to the conversion efficiency $\theta_{j_c \to j_s}$ from the charge current to the SC. In general, an SC source with a two-dimensional geometry, such as an interfacial SOI, suppresses $\theta_{j_s \to j_c}$ rather than $\theta_{j_c \to j_s}$ although the value of $\theta_{j_c \to j_s}/\theta_{j_s \to j_c}$ cannot exceed 10[49,50]. If the SC source does produce such a geometrical effect in the Si/Al gradient material, the non-reciprocity is expected to be intermediate between that of a bulk and an interfacial SOI because of its fuzzy interface. However, as shown in Fig. 4a, the sample with $t_i = 0.5$ nm exhibits a $\xi_{DL}/\theta_{j_s \to j_c}$ value much larger than 10. On the other hand, $\xi_{DL}/\theta_{j_s \to j_c}$ for $t_i = 0$ nm is unity, at which the highest two-dimensional geometry is expected. The fact that strong non-reciprocity is observed, not for $t_i = 0$ nm but for $t_i = 0.5$ nm, therefore suggests that the SC is generated by neither interfacial SOI nor inversion symmetry breaking at the Si/Al interface, but by angular momentum conversion from macroscopic vorticity in the electric current at the compositional gradient.

Figure of merit for spin torque switching capability of Si/Al gradient materials

To suppress the power-supply voltage for spin torque switching, the product of ξ_{DL} and the electrical conductivity σ_e of the NM must increase. Moreover, the magnitude of σ_e itself should increase to reduce resistive-capacitive delays, which hinder the high-speed operation of integrated circuits. The relative abundance of elements P_n is also an important parameter for sustainable development of SC-generating materials. To satisfy these demands, a figure of merit (FOM) for SC-generating materials can be determined as the product of these values as follows:

$$FOM = (\xi_{DL}\sigma_e) \times \sigma_e \times P_n = [\text{Spin torque efficiency}] \times [\text{Circuit performance}] \times [\text{Element sustainability}] \tag{3}$$

From the statistical data for P_n in Fig. 1a, $P_{Si/Al} = P_{Si} \times P_{Al} = 2.24 \times 10^{-2}$, which is seven orders of magnitude larger than the value for Pt (P_{Pt} of 5×10^{-9}). Si/Al gradient materials therefore offer a highly superior solution for sustainable materials development. Figure 4b displays a double logarithmic graph with respect to σ_e and $\xi_{DL}\sigma_e$ for the Si/Al gradient samples. The data for a Pt/Ni$_{95}$Cu$_5$ bilayer film are also plotted as a closed square for comparison. σ_e is shown as a function of t_i in Supplementary note S8. The dashed lines in Fig. 4b represent contours of $\xi_{DL}\sigma_e^2$. In addition to $\xi_{DL}\sigma_e$, we can also increase σ_e in our Si/Al gradient materials by decreaseing t_i from 2.0 to 0.5 nm. This is surprising because strong SOI materials such as Pt, W, and Ta, typically exhibit low σ_e. More specifically, $\xi_{DL}\sigma_e^2$ can be larger than the typical value for strong-SOI materials even at the same value of ξ_{DL}. Indeed, we achieved a $\xi_{FMR}\sigma_e^2$ value of 14.3 $(MS/m)^2$ for $t_i = 0.5$ nm, which is seven times larger than that in Pt. Moreover, the FOM for this material was 3.2×10^{11} $(S/m)^2$, which is seven orders of magnitude greater than that of Pt (1.0×10^4 $(S/m)^2$). The overwhelmingly higher FOM for our fabricated films demonstrates the high potential for Si/Al gradient materials to be widely used in low-energy consumption and sustainable spin devices.
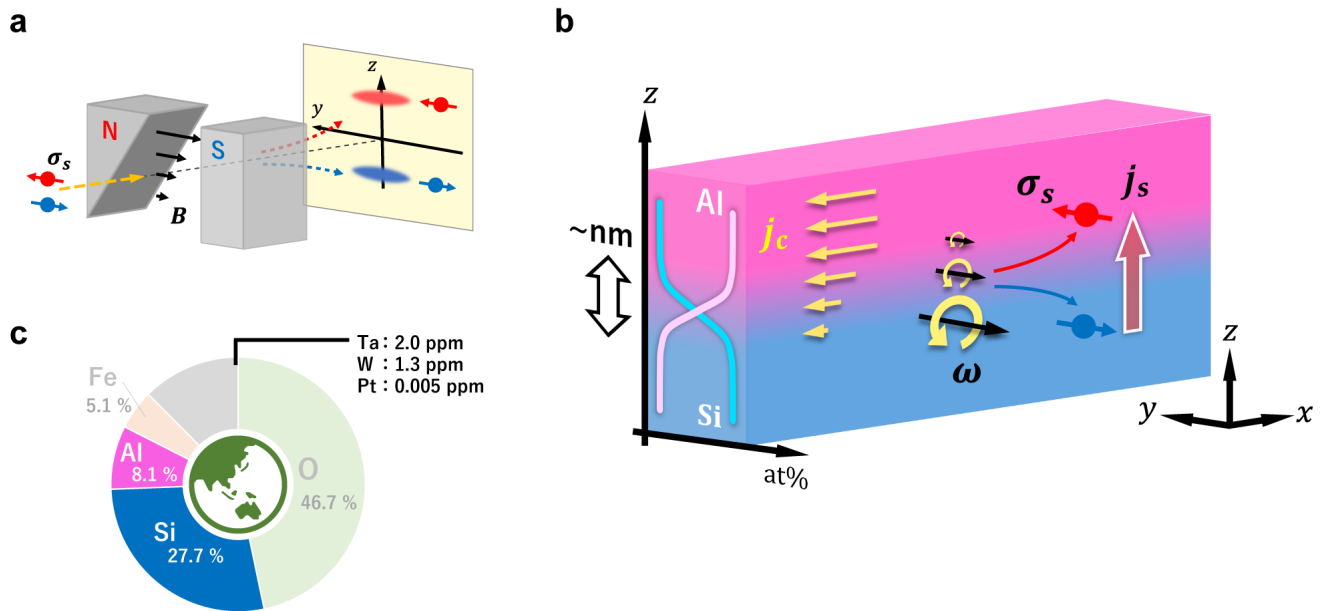
Fig. 1 | Green and rare-metal-free composition gradient material for spin current generation.
a, Schematic illustration of the Stern-Gerlach experiment. Quantisation of spin angular momentum $\boldsymbol{\sigma}_s$ was observed when a beam of silver atoms was split in two as it passed through a gradient of a static magnetic field $\boldsymbol{B}$. **b**, Schematic image of a fabricated Si/Al gradient material. The Cartesian coordinate system used throughout this article is also shown in (**b**). A nanometre-thick compositional gradient from Si to Al exists along the z-axis with much conductivity in the Al layer than the Si layer. When an electric current $\boldsymbol{j}_c$ is applied along the x-axis, an electric current vorticity $\boldsymbol{\omega} = \nabla \times \boldsymbol{j}_c$ appears, whose vector points along the y-axis. The electron spin $\boldsymbol{\sigma}_s$ in the gradient material is polarised along the y-axis by an emergent magnetic field due to the vortical electric current. As a consequence, the gradient of $\boldsymbol{\omega}$ leads to a density gradient in the non-equivalent electron spin, which produces a spin current along the z-axis. **c**, A plot of relative elemental abundance in the Earth's crust. Si and Al represent the most abundant semiconductor and metal materials, respectively, while typical large spin current source materials such as Ta, W, and Pt are very rare.
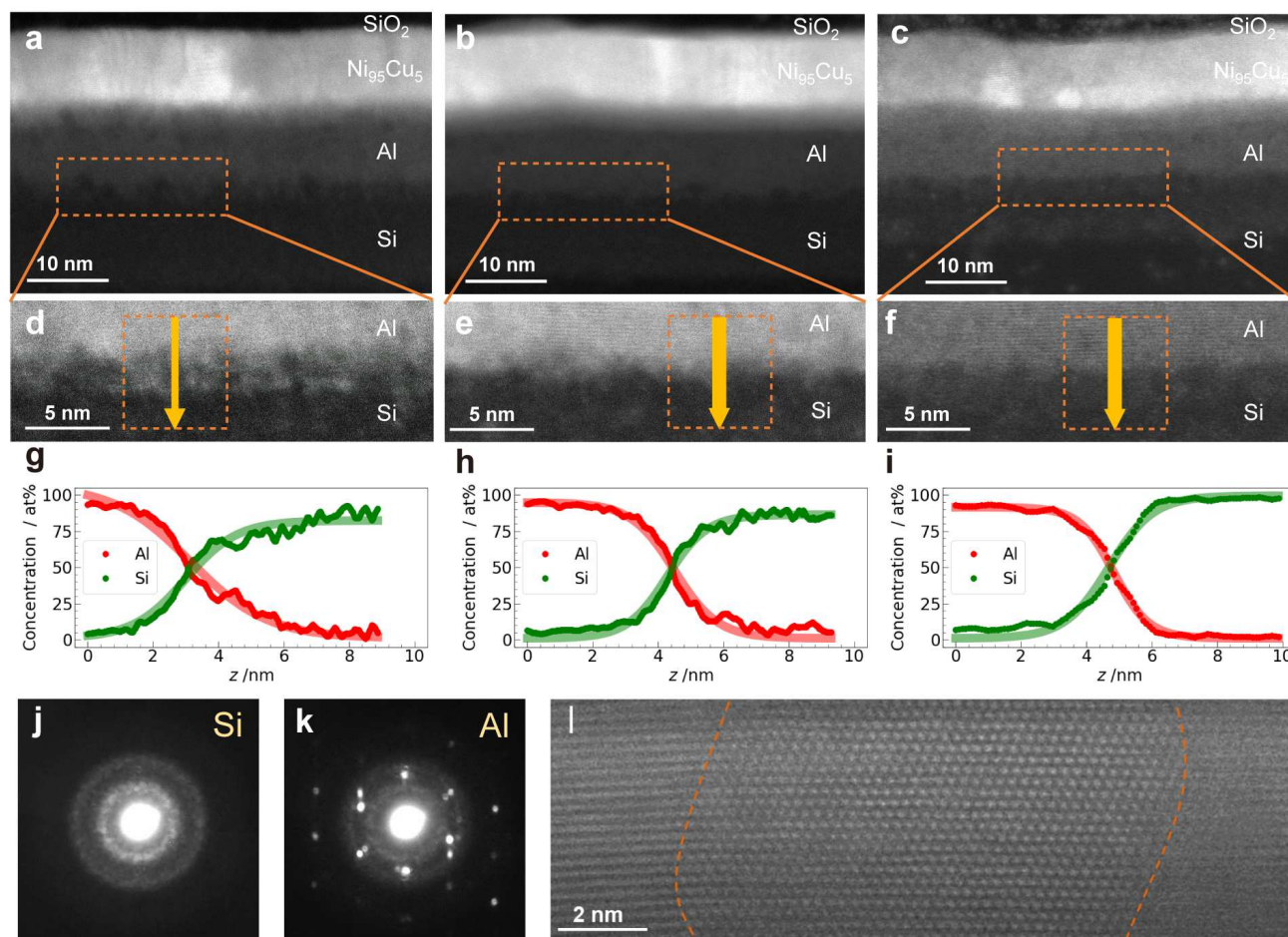
Fig. 2 | Microstructural and compositional characterisation of gradients across the Si/Al interface. a-c, HAADF-STEM images of samples with (**a**) $t_i = 2.0$, (**b**) 1.0, and (**c**) 0.0 nm. **d-f**, Enlarged views of the sample near the area analysed by EDS. EDS profiles were generated from within the orange dashed boxes. **g-i**, Averaged profiles of the atomic concentration of Si and Al for each sample along the arrows in each box. **j,k**, Nanobeam diffraction patterns for Si and Al layers, respectively. **l**, High-resolution HAADF-STEM image of the Al layer. Dashed lines indicate the grain boundaries.
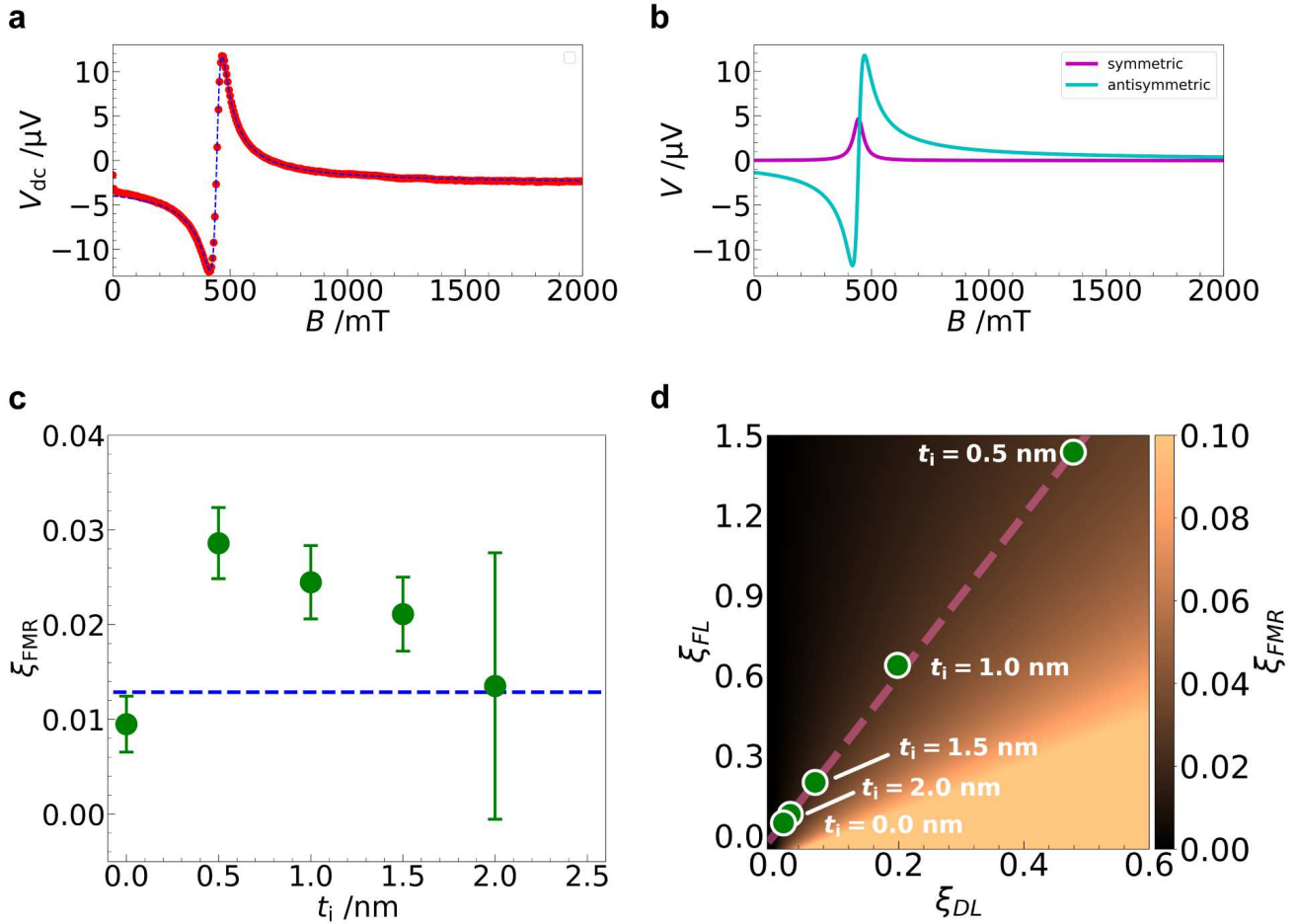
Fig. 3 | ST-FMR experiment for evaluating electric-current-induced spin torque. a, ST-FMR spectrum measured for a Si/Al/Ni$_{95}$Cu$_5$ trilayer film with $t_i = 0.5$ nm at a microwave frequency of 20 GHz. The dashed curve represents the best-fit result for a combination of symmetric- and antisymmetric-Lorentzian functions. **b**, Symmetric (purple) and antisymmetric (blue) Lorentzian components included in (**a**). **c**, Spin torque efficiency ξ_{FMR} as a function of t_i. The vertical bars indicate the standard deviation calculated from the least-squares deviation of the fitting parameters used in the caluculation of ξ_{FMR}. The closed circles indicate the ξ_{FMR} values of samples with t_i ranging from 0 to 2.0 nm. The horizontal dashed line shows the ξ_{FMR} for a reference sample with an Al(10 nm)/Ni$_{95}$Cu$_5$(10 nm) structure. **d**, Colour plot of ξ_{FMR} as a function of ξ_{DL} and ξ_{FL}. The dashed line indicates the condition $\xi_{FL} = 3\xi_{DL}$, which was determined by measuring the Ni$_{95}$Cu$_5$ layer thickness dependence of ξ_{FMR} for a sample with $t_i = 1.0$ nm (see Supplementary note S3). The closed circles are each labelled with the t_i value.
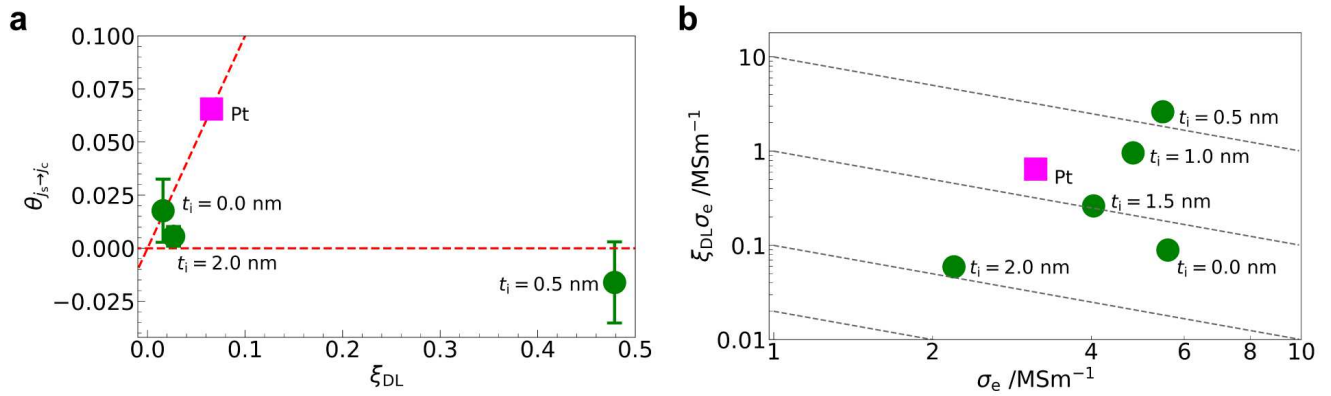
Fig. 4 | Figure of merit for Si/Al gradient material. a, Conversion efficiency from SC to charge current $\theta_{j_s \to j_c}$ as a function of ξ_{DL}. The circles show data for samples with various t_i, whereas the square represents values for a Pt(10 nm)/Ni$_{95}$Cu$_5$(10 nm) bilayer film. The vertical bars indicate the standard deviation calculated from the leaset-squares deviation of the fitting parameters used to calculate $\theta_{j_s \to j_c}$. **b**, Double logarithmic plot of electric conductivity σ_e and $\xi_{DL}\sigma_e$ for samples with t_i ranging from 0 to 2.0 nm. The data for a Pt(10 nm)/Ni$_{95}$Cu$_5$(10 nm) bilayer film is also plotted for comparison(square). Dashed lines are contours of $\xi_{DL}\sigma_e^2$.

Methods

Sample Preparation

The films were fabricated on thermally oxidised silicon substrates by magnetron sputtering at room temperature. The chamber base pressure prior to deposition was less than 5.0×10^{-4} Pa. The deposition pressure was 0.22 Pa with an argon (Ar) flow rate of 4.0 sccm. The Al layer creation used radio-frequency (RF) deposition at 13.56 MHz with a power density of 1.4 W/m^2 and a deposition rate of 0.043 nm/s from a 99.9%-pure Al target. The Si layer was deposited by RF-sputtering with a power density of 3.5 W/m^2 and a deposition rate of 0.062 nm/s from a non-doped Si target. The Ni$_{95}$Cu$_5$ layer was deposited by direct current (DC) sputtering with a power density of 1.4 W/m^2 and a deposition rate of 0.2 nm/s from a 99.9%-pure Ni$_{95}$Cu$_5$ alloy target. The SiO$_2$ capping layer was deposited by RF-sputtering with a power density of 3.5 W/m^2 and a deposition rate of 0.044 nm/s from a 99.99%-pure SiO$_2$ target. The thin films were patterned into strips 10-μm-wide and 100-μm-long by photolithography and lift-off processes. An electrically shorted coplanar waveguide made from 70-nm-thick Au was connected to both ends of the strip to conduct the ST-FMR measurements. All measurements were conducted at room temperature.

Electrical Measurements

For ST-FMR measurements, we applied 20-dBm continuous sinusoidal signals with a frequency of 20 GHz in the longitudinal direction (x-axis) of the film by a signal generator. An in-plane external magnetic field was applied with an amplitude ranging from 0 to 2.0 T at a fixed angle of $\pi/4$ with respect to the x-axis. We then measured the rectified DC voltage V_{dc} by a nanovoltmeter from a DC port of bias tee. The resulting spectra were fit by the expression $V_{dc} = V_s f_s(B) + V_a f_a(B)$, where $f_s(B)$ and $f_a(B)$ are the symmetric- and antisymmetric-Lorentzian functions, respectively. The inverse SHE measurement used a general spin-pumping experiment setup. We applied a continuous sinusoidal signal with amplitude of 20 dBm and a frequency of 5 GHz into the coplanar waveguide fabricated on the sample, which was patterned into a Hall-bar shape. The sample and coplanar waveguide were insulated by the insertion of 120-nm-thick SiO$_2$ film. The external magnetic fields with amplitudes ranging from 0 to 2.0 T were applied in the x-y plane at an angle ranging between 0 and 2π from the x-axis. The DC inverse spin Hall voltage was measured using a nanovoltmeter.

Electron microscopy characterisation

We prepared cross-sectional thin specimens for HAADF-STEM characterisation using a focused ion beam with a Ga$^+$ ion source on a FEI Helios G4 UX instrument. Before the milling process, a $\sim$5 nm-thick Au layer was deposited on the film surface to protect and enhance the conductivity of sample during milling. The lift-out lamellae were thinned to $\sim$100 nm at 30 kV with a current decreasing from 0.75 nA to 90 pA, followed by final polishing at 2 kV and 17 pA. HAADF-STEM and NBED images were obtained using a Cs-corrected FEI Titan G2 80–200 equipped with a Super-X EDS. The HAADF-STEM images were collected using a convergence semi-angle of 18 mrad and an inner-collection semi-angle of 55 mrad. EDS mapping was performed using a Bruker Esprit analysis system with automatic drift correction during the collection process, which augments the reliability of the compsitional analysis. Integrated line profiles were conducted across the heterostructure in EDS maps to enhance the signal-to-noise ratio. The Cliff–Lorimer analysis method was applied to quantify the EDS line-scan results.

References

1. Chappert, C., Fert, A., and Van Dau, F. N. The emergence of spin electronics in data storage. *Nat. Mater.* **6**, 813 (2007).

2. Tudu, B., and Tiwari, A. Recent developments in perpendicular magnetic anisotropy thin films for data storage applications. *Vacuum* **146**, 329 (2017).

3. Liu, L., Pai, CF., Ralph, D. C., and Buhrman, R. A. Magnetic oscillations driven by the spin Hall effect in 3-terminal magnetic tunnel junction devices. *Phys. Rev. Lett.* **109**, 186602 (2012).

4. Demicov, V. E. et al. Magnetic nano-oscillator driven by pure spin current. *Nat. Mater.* **11**, 1028-1031 (2012).

5. Duan, Z. et al. Nanowire spin torque oscillator driven by spin orbit torques. *Nat. Commun.* **5**, 5616 (2014).

6. Hirsch, J. E. Spin Hall effect. *Phys. Rev. Lett.* **83**, 1834 (1999).

7. Zang, S. Spin Hall effect in the presence of spin diffusion. *Phys. Rev. Lett.* **85**, 393 (2000).

8. Valenzuela, S. O., and Tinkham, M. Direct electronic measurement of the spin Hall effect. *Nature* **442**, 176 (2006).

9. Maekawa, S. A flood of spin current. *Nat. Mater.* **8**, 777 (2009).

10. Kato, Y. K., Myers, R. C., Gossard, A. C., and Awschalom, D. D. Observation of the spin Hall effect in semiconductors. *Science* **306**, 1910 (2004).

11. Edelstein, V. M. Spin polarization of conduction electrons induced by electric current in two-dimensional asymmetric electron systems. *Solid State Commun.* **73**, 233 (1990).

12. Ganichev, S. D. Spin-galvanic effect. *Nature (London).* **417**, 153 (2002).

13. Rojas Sánchez, J. C. et al. Spin-to-charge conversion using Rashba coupling at the interface between non-magnetic materials. *Nat. Commun.* **4**, 2944 (2013).

14. Manchon, A., Koo, H. C., Nitta, J., Frolov, S. M., and Duine, R. A. New perspectives for Rashba spin–orbit coupling. *Nat. Mater.* **14**, 871 (2015).

15. Liu, L. et al. Spin-torque switching with the giant spin Hall effect of tantalum. *Science* **336**, 555 (2012).

16. Allen, G., Manipaturuni, S., Nikonov, D. E., Doczy, M., and Young I. A. Experimental demonstration of the coexistence of spin Hall and Rashba effects in β-tantalum/ferromagnet bilayers. *Phys. Rev. B* **91**, 144412 (2015).

17. Yu, R. et al. Determination of spin Hall angle and spin diffusion length in β-phase-dominated tantalum. *Phys. Rev. Mater.* **2**, 074406 (2018).

18. Pai, CF. et al. Spin transfer torque devices utilizing the giant spin Hall effect of tungsten. *Appl. Phys. Lett.* **101**, 122404 (2012).

19. Hao, Q., and Xiao, G. Giant Spin Hall Effect and Switching Induced by Spin-Transfer Torque in a W/$Co_{40}Fe_{40}B_{20}$/MgO Structure with Perpendicular Magnetic Anisotropy. *Phys. Rev. Appl.* **3**, 034009 (2015).

20. Gerlach, W., and Stern, O. Der experimentelle nachweis der richtung-squantelung im magneticfield. *Z. Phys.* **9**, 349–352 (1922).

21. Gerlach, W., and Stern, O. Das magnetische moment des silber atoms. *Z. Phys.* **9**, 353–355 (1922).

22. Takahashi, R. et al. Spin hydrodynamic generation. *Nat. Phys.* **12**, 52-56 (2016).

23. Kobayashi, D. et al. Spin current generation using a surface acoustic wave generated via spin-rotation coupling. *Phys. Rev. Lett.* **119**, 077202 (2017) .

24. Kurimune, Y., Matsuo, M., Maekawa, S., and Nozaki, Y. Highly nonlinear frequency-dependent spin-wave resonance excited via spin-vorticity coupling. *Phys. Rev. B* **102**, 174413 (2020).

25. Tateno, S., Okano, G., Matsuo, M., and Nozaki, Y. Electrical evaluation of the alternating spin current generated via spin-vorticity coupling. *Phys. Rev. B* **102**, 104406 (2020).

26. The STAR Collaboration. Global Λ hyperon polarization in nuclear collisions. *Nature* **548**, 62–65 (2017).

27. Petersen, H. The fastest-rotating fluid. *Nature* **548**, 34-35 (2017).

28. Okano, G., Matsuo, M., Ohnuma, Y., Maekawa, S., and Nozaki, Y. Nonreciprocal spin current generation in surface-oxidized copper films. *Phys. Rev. Lett.* **122**, 217701 (2019).

29. An, H., Kageyama, Y., Kanno, Y., Enishi, N., and Ando, K. Spin–torque generator engineered by natural oxidation of Cu. *Nat. Commun.* **7**, 13069 (2016).

30. Kageyama, Y. et al. Spin-orbit torque manipulated by fine-tuning of oxygen-induced orbital hybridization. *Sci. Adv.* **5**, eaax4278(2019).

31. Gao, T. et al. Intrinsic spin-orbit torque arising from the Berry curvature in a metallic-magnet/Cu-oxide interface. *Phys. Rev. Lett.* **121**, 017202 (2018).

32. Kim, J. et al. Nontrivial torque generation by orbital angular momentum injection in ferromagnetic-metal/Cu/Al_2O_3 trilayers. *Phys. Rev. B* **103**, L020407 (2021).

33. Liu, L., Moriyama, T., Ralph, D. C., and Buhrman, R. A. Spin-Torque Ferromagnetic Resonance Induced by the Spin Hall Effect. *Phys. Rev. Lett.* **106**, 036601 (2011).

34. Mosendz, O. et al. Detection and quantification of inverse spin Hall effect from spin pumping in permalloy/normal metal bilayers. *Phys. Rev. B.* **82**, 214403 (2010).

35. Pai, CF., Ou, Y., Valelaleão, L. H., Ralph, D. C., and Buhrman, R. A. Dependence of the efficiency of spin Hall torque on the transparency of Pt/ferromagnetic layer interfaces. *Phys. Rev. B* **92**, 064426 (2015).

36. Harder, M., Gui, Y., and Hu, CM. Electrical detection of magnetization dynamics via spin rectification effects. *Phys. Rep.* **661**,1 (2016).

37. Sklenar, J. et al. Unidirectional spin-torque driven magnetization dynamics. *Phys. Rev. B.* **95**, 224431 (2017).

38. Horaguchi, T., Matsuo, M., and Nozaki, Y. Highly accurate evaluation of spin-torque efficiency by measuring in-plane angular dependence of spin-torque ferromagnetic resonance. *J. Magn. Magn. Mater.* **505**, 166727 (2020).

39. Hoffman, A.. Spin Hall effects in metals. *IEEE Trans. Magn.* **49** 5172 (2013).

40. Amin, V. P., Zemen, J., Stiles, M. D. Interface-generated spin currents. *Phys. Rev. Lett.* **121**, 136805 (2018).

41. Matsuo, M., Ohnuma, Y., Maekawa, S. Theory of spin hydrodynamic generation. *Phys. Rev. B* **96**, 020401(R) (2017).

42. Matsuo, M., Ieda, J., Harii, K., Saitoh, E., and Maekawa, S. Mechanical generation of spin current by spin-rotation coupling. *Phys. Rev. B* **87**, 180402(R) (2013).

43. Saitoh, E., Ueda, M ., Miyajima, H., and Tatara, G. Conversion of spin current into charge current at room temperature: Inverse spin-Hall effect. *Appl. Phys. Lett.* **88**, 282509 (2006).

44. Zhao, H., Loren, E. J., van Driel, H. M., and Smirl L. Coherence control of Hall charge and spin currents. *Phys. Rev. Lett.* **96**, 246601 (2006).

45. Tserkovnyak, Y., Brataas, A., Bauer G. E. W. Enhanced Gilbert damping in thin ferromagnetic films. *Phys. Rev. Lett.* **88**, 117601 (2002).

46. Wang, H. L. et al. Scaling of Spin Hall Angle in 3d, 4d, and 5d Metals from $Y_3Fe_5O_{12}$/Metal Spin Pumping. *Phys. Rev. Lett.* **112**, 197201(2014).

47. Ando, K. et al. Inverse spin-Hall effect induced by spin pumping in metallic system. *J. Appl. Phys.* **109**, 103913 (2011).

48. Shikoh, E. et al. Spin-Pump-Induced Spin Transport in p-Type Si at Room Temperature. *Phys. Rev. Lett.* **110**, 127201 (2013).

49. Deorani, P. et al. Observation of inverse spin Hall effect in bismuth selenide. *Phys. Rev. B* **90**, 094403 (2014).

50. Wang, Y. et al. Topological Surface States Originated Spin-Orbit Torques in Bi_2Se_3. *Phys. Rev. Lett.* **114**, 257202 (2015).

Acknowledgements

Author contributions

T.H. and Y.N. planned the study and wrote the manuscript. T.H. performed film deposition and fabricated the devices. C.H. and T.O. performed the microscopy experiments with the help of K.H. T.H. carried out the measurements and analysed the data with the help of K.Y. and Y.N. T.H., J.F., M.M., and Y.N. performed the numerical calculation based on SVC theory. All the authors discussed the results and commented on the manuscript.

Supplementary Files

This is a list of supplementary files associated with this preprint. Click to download.

- SiAlSupplementaryver4.3.pdf